ACS Biomaterials SCIENCE & ENGINEERING Article
Cite This: ACS Biomater. Sci. Eng. 2018, 4, 1916−1923

Role of Extracellular Matrix in the Biomechanical Behavior of Pancreatic Tissue

Alexa W. Hudnut,[†] Lian Lash-Rosenberg,[‡] An Xin,[§] Juan A. Leal Doblado,[∥] Cecilia Zurita-Lopez,[∥] Qiming Wang,[§] and Andrea M. Armani*[,†,⊥]

[†]Department of Biomedical Engineering, [‡]Department of Mechanical Engineering, and [⊥]Mork Family Department of Chemical Engineering and Materials Science, University of Southern California, 1002 Childs Way, MCB 495, Los Angeles, California 90089, United States

[§]Department of Civil Engineering, University of Southern California, 920 Downey Way, BHE 222, Los Angeles, California 90089, United States

[∥]Department of Chemistry and Biochemistry, California State University Los Angeles, 617 Charles E. Young Drive E, Room 251, Los Angeles, California 90095, United States

Supporting Information

ABSTRACT: Correlating the biomechanical properties of tissue with its function is an emerging area of research with potential impact in diagnostics, therapeutics, and prognostics. A critical stepping-stone in developing structure−function models is creating methods that can correlate the tissue structure with its mechanical behavior. As an initial step in addressing this challenge, we have characterized the mechanical behavior of unprocessed pancreatic tissue using optical fiber polarimetric elastography. To correlate the observed behavior to physiologically relevant structural features, a series of architectures are designed and fabricated using 3D printing. The mechanical response of the 3D printed elastomeric structures is analyzed using compressive testing and modeled using finite element analysis. The biomechanical behavior and buckling point of the 3D printed structures is used to create a calibration curve to understand the measured response of the resected pancreatic tissue. Based on the modeling and biomimetic results, the biomechanical behavior of pancreatic tissue is likely due to the collagen IV network.

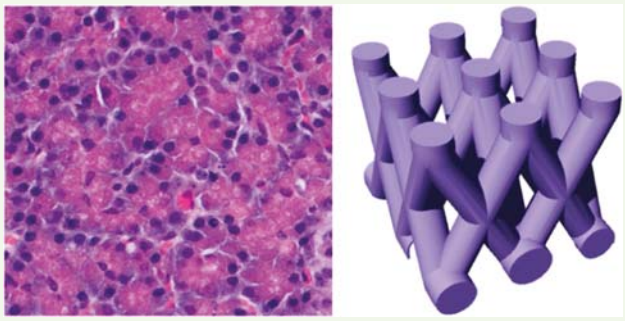

KEYWORDS: *3D printing, biomechanics, elastography, polarimetry, Young's modulus, FEA modeling*

1. INTRODUCTION

The biomechanical characteristics of tissue are increasingly being implicated in the development of both chronic and acute diseases.[1] Diseases as diverse as cancer, blast induced traumatic brain injury (bTBI), and heart disease all are known to involve the stiffening of tissue.[2−4] However, in all of these cases, little is understood about how the structural changes directly correlate to the tissue's function.[5,6] By creating advanced analytical methods and techniques for characterizing living tissue, improved models of disease progression across a variety of chronic and acute diseases can be developed. Eventually, these models could be used to design preventative therapeutics by identifying and treating the pathologies earlier in the progression of the disease.

However, studying the mechanics of living tissue is challenging due to the complex structure of the tissue. For example, the extracellular matrix (ECM) is a three-dimensional structure comprised of interconnected cells and a network of supporting scaffolds that have a wide range of viscoelastic properties.[3,7,8] In order to understand the mechanical behavior of tissue, methods must capture the tissue as a whole, as well as the micron-scale heterogeneity. Conventional mechanical characterization methods developed for viscoelastic material analysis are optimized for a single length scale. An additional challenge is that the mechanical behavior of tissue changes over time due to cellular death and autolysis. These changes begin immediately after a tissue section has been excised. As such, the biomechanical analysis of resected tissue must be performed within the first 2 h after resection, before the onset of rigor mortis.[9] This limits the extent of mechanical behavior characterization that can be performed on the tissue. Therefore, researchers have focused efforts on understanding the structure of tissue through imaging and chemical characterization.

Several imaging methods including immunohistochemistry, multiphoton microscopy, and confocal microscopy have been used to characterize tissue structure.[5,10−15] For all imaging and

Received: March 21, 2018
Accepted: March 27, 2018
Published: March 27, 2018

chemical characterization measurements, the tissue samples must undergo significant processing, including staining and fixing with additional reagents. These processes are time-consuming and may impact the structure of the tissue. Immunohistochemistry (IHC) is a form of imaging that enables specific biomarkers indicative of stiffness to be selected and imaged.[5,10,11] IHC is limited by the fact that the biomarkers must be known before conducting experiments. Second harmonic generation imaging (SHG) is an alternative method of imaging that can be used to resolve the ECM structure within the tissue without having to target specific biomarkers using fluorescent probes. SHG has been used extensively to visualize collagen within different tissues.[5,11,12] In addition to being able to take 2D images of tissue, 3D images can be reconstructed using techniques such as confocal microscopy. The 3D reconstructions of mm scale samples provide information about the structure of the ECM with μm resolution.[13−15] Ultimately, for all imaging techniques, the biggest limitation is that the results are static. Thus, there is no way to measure the dynamic mechanical response of the structures to mechanical interrogation.

Mechanical analysis methods offer significant advantages over imaging because a range of mechanical characteristics can be studied by modifying the experimental parameters. Examples of mechanical properties include buckling, bridging, and delamination.[16−18] One approach for categorizing mechanical analysis methods is to evaluate their compatibility and utility for analyzing complex biological samples. Methods such as rheology, sonoelastography, and optical coherence elastography are able to measure the ECM but tend to have lower resolution.[19−21] Methods such as atomic force microscopy (AFM) have nm resolution allowing individual cells to be studied, but they are unable to measure the dynamic mechanical behavior of intact ECM structure.[22] This limitation is primarily due to the fact that AFM is not suitable for analyzing the large-scale mechanical deformations that the ECM networks undergo and that are characteristic of individual tissues.

To address these limitations, optical fiber polarimetric elastography (OFPE) has emerged as a method of high resolution mechanical testing of biomaterials that is able to capture the global tissue mechanics despite the heterogeneity of the ECM composition.[23−25] In addition to the Young's modulus, OFPE can detect dynamic mechanical behaviors such as buckling and hysteresis. Therefore, OFPE can be used to measure the biomechanical behavior of tissue before the onset of rigor mortis.

In parallel, significant advances in fabricating biomimetic structures have occurred. Several methods exist, including directly writing with elastomeric and hydrogel inks, casting hydrogels, and lithographic etching of silicone elastomer.[26−28] While they all have advantages, they are limited in the resolution and complexity of the geometries they can create. Recently, an alternative method for creating biomimetic structures with nearly arbitrary geometries was developed based on indirect 3D printing. In this method, an inverse mold of the desired biomimetic structure was 3D printed.[29] This approach enables a significantly wider range of materials to be fabricated, as the materials are no longer directly patterned using etching or UV illumination.

In the present work, we design and fabricate 3D printed elastomeric structures based on imaging and perform finite element analysis (FEA) modeling of their mechanical behavior. These results are compared to OFPE analysis of pancreatic tissue, allowing the primary structure governing the dominant biomechanical behavior to be identified. The biomimetic structure design is based on past results in the literature, and confirmed for the specific pancreas samples mechanically tested with pathology imaging.[30] By combining model and real systems, we are able to address gaps in the understanding of tissue biomechanics.[16,31] We focus the biomechanical comparison on the buckling point of the two different material systems, and we perform complementary FEA modeling to quantify the relative contributions of the different structural elements. OFPE results are used as physiological guidelines to determine the accuracy of the modeling results.

2. THEORY

It is well-known that the geometry of viscoelastic materials has a significant impact on their mechanical response.[29,32,33] In order to understand the elastic behavior of a structure, a series of analytical functions can be used to describe the mechanical behavior of the material in terms of a strain energy function[34]

$$W = \sum_{i+j+k=1}^{\infty} C_{ij}(I_1 - 3)^i \cdot (I_2 - 3)^j \cdot (I_3 - 1)^k \tag{1}$$

where I_1, I_2, and I_3 are the strain invariants of the Green's deformation tensor. Within this relationship, I_1, I_2, and I_3 can be defined, and λ_i is a distinct principle extension ratio:[34]

$$I_1 = \lambda_1^2 + \lambda_2^2 + \lambda_3^2 \tag{2}$$

$$I_2 = \lambda_1^2\lambda_2^2 + \lambda_2^2\lambda_3^2 + \lambda_3^2\lambda_1^2 \tag{3}$$

$$I_3 = \lambda_1^2\lambda_2^2\lambda_3^2 \tag{4}$$

The biomimetic structures are fabricated from a hyperelastic material and thus are incompressible. Therefore, $I_3 = 1$ since it represents the compressibility of the material within the tensor. Eq 1 can be simplified to[34]

$$W = \sum_{i+j=1}^{\infty} C_{ij}(I_1 - 3)^i \cdot (I_2 - 3)^j \tag{5}$$

To fit the results to a neo-Hookean model, the strain energy function is derived from the reduced polynomial model. Eq 5 thus must be modified to reflect this change[35]

$$W = \sum_{i=1}^{N} C_{i0}(\overline{I}_1 - 3)^i + \sum_{i-1}^{N} \frac{1}{D_i}(J_{el} - 1)^{2i} \tag{6}$$

where $j = 0$, J_{el} is the elastic volume ratio, $\overline{I}_1$ is the first invariant of the deviatoric strain, and N is the number of terms in the strain energy function. The material constants C_{i0} and D_i describe the shear behavior and the compressibility of the material, respectively.

3. MATERIALS AND METHODS

3.1. Pancreatic Tissue Sample Preparation. To obtain pancreatic tissue samples, surgical fellows resect sections of porcine pancreatic tissue from animals under anesthesia (University of Southern California IACUC Approval-10843). The organ samples are then placed in RPMI media (Gibco, RPMI 1640) without any additives and put on ice until testing. The samples are stored for less than 2 h to ensure that the tested biomechanical properties accurately reflect that of the unresected tissue. Alternative culture media without additives, such as DMEM, could be used since the tissue is stored for

DOI: 10.1021/acsbiomaterials.8b00349
ACS Biomater. Sci. Eng. 2018, 4, 1916−1923

less than 2 h and is not frozen. Individual sections with dimensions of 7 mm × 7 mm × 4 mm (lxwxh) are cut for imaging and compressive testing.

For imaging purposes, the pancreatic tissues are fixed in 10% neutral buffered formalin for 24−30 h, paraffin-embedded, and sectioned at 5 μm thickness. A hematoxylin and eosin (H&E) stain is performed according the manufacturer's instructions (Leica Biosystems). The stained sections are then imaged using a light microscope. An example of the images obtained after H&E staining is shown in Figure 1a. All mechanical testing is completed on unprocessed tissue samples within the delay period before the onset of rigor mortis, which corresponds to the first 2 h after resection.

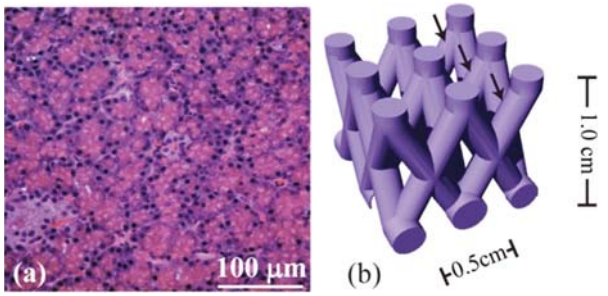

Figure 1. Images of pancreatic tissue are used to determine the physical structure of the biomimics. (a) Sections of pancreatic tissue are stained with hematoxylin and eosin and imaged using a light microscope. (b) Based on these parameters, simplified structures are drawn in SolidWorks and used for fabricating biomimetic structures and computer modeling.

3.2. Biomimetic Structure Design. Based on past imaging studies that have identified the ECM structure of pancreatic tissue, a simplified structure is designed in SolidWorks (Figure 1b).[5,10−15,30] Pathology imaging results are used to confirm that the geometry of mechanically tested pancreas samples is consistent with past results (Figure 1a). The design used for the ECM of pancreatic tissue is an orthorhombic crystal structure with an interconnecting support lattice.

Five variants on the base structure are designed by changing the diameter (D) of the beams while holding the length (L) constant, providing a range of diameter to length ratio (D/L) values spanning from 0.11 to 0.25. The criteria for selecting the D/L range are based on previously published IHC, SHG, and SEM imaging results of the ECM of pancreatic tissue.[5,10,11,30] Based upon these results, we determined a range of values from 0.11 to 0.25 would likely include the physiological range of ECM thickness and would provide the information necessary to determine the primary biomechanical behavior of the structure.

An additional five variants on the base structure, resulting in six total structures, are designed by systematically removing different support beams, as indicated by the arrows in Figure 1b. The variations on the geometry were selected in a systematic way that mimics the methods used in crystallography research.[36] Changes were limited to the support of one face of the structure, and the beams were sequentially removed to better understand how each contributes to total load bearing. In this set of designs, the D/L ratio is held fixed at 0.25.

3.3. FEA Modeling of the Mechanical Behavior. The buckling behaviors of the biomimetic structures are modeled using commercial FEA software, Abaqus FEA. The material is taken to obey the neo-Hookean model. The compression test is modeled with strain-controlled loading. The Riks model is employed to capture the buckling and postbuckling behaviors. Mesh refinement studies are performed to ensure the accuracy of the results. The buckling point is identified as the critical point of the stress−strain curve of the structure.

The lattice is comprised of a neo-Hookean material, where the material coefficients are 0.5 (C_i0) and 0.1 (D_i), respectively. A displacement of 0.5 mm is applied to the top surface of the part to simulate a compressive load that generates a large deformation. A mesh of 0.9 mm is applied to the structure. According to the structural symmetry, boundary conditions are built along the five planes of symmetry, and only a small part of the lattice is modeled. This allows us to decrease the computational cost.

3.4. Biomimetic Structure Fabrication. Projection microstereolithography is used to 3D print the biomimetic structures. First, the precise geometries are defined in SolidWorks. These are used to 3D print hollow scaffolds using projection microstereolithography. The scaffolds are printed from a photoresin comprised of *N*,*N*-dimethylacrylamide (40 wt %), methacrylic acid (40 wt %), methacrylic anhydride (7 wt %), polyvinylpyrrolidone (11 wt %), 2,4,6-trimethylbenzoyl, and phosphine oxide (2 wt %).[29,37] The stereolithography system prints a single 2D slice of the structure, using UV light to cure each photoresin layer. This process is performed iteratively until the entire scaffold has been created. The structure is printed on a glass stage build plate, which is submerged in a solution well. The solution well is protected by a thin oxygen permeable membrane to prevent adhesion between the resin and the solution well by creating an oxygen rich zone that inhibits photopolymerization.[29]

Once completed, the scaffold is dried in ambient lab conditions for 2 h (Figure 2a/b). Then the scaffold is filled with a tin-catalyzed silicone elastomer (Mold Max NV14) using a syringe pump (Figure 2c/d). A mixture of a 10:1 ratio of base to cross-linker, by weight, is used for the silicone elastomer. Once filled, the silicone elastomer is

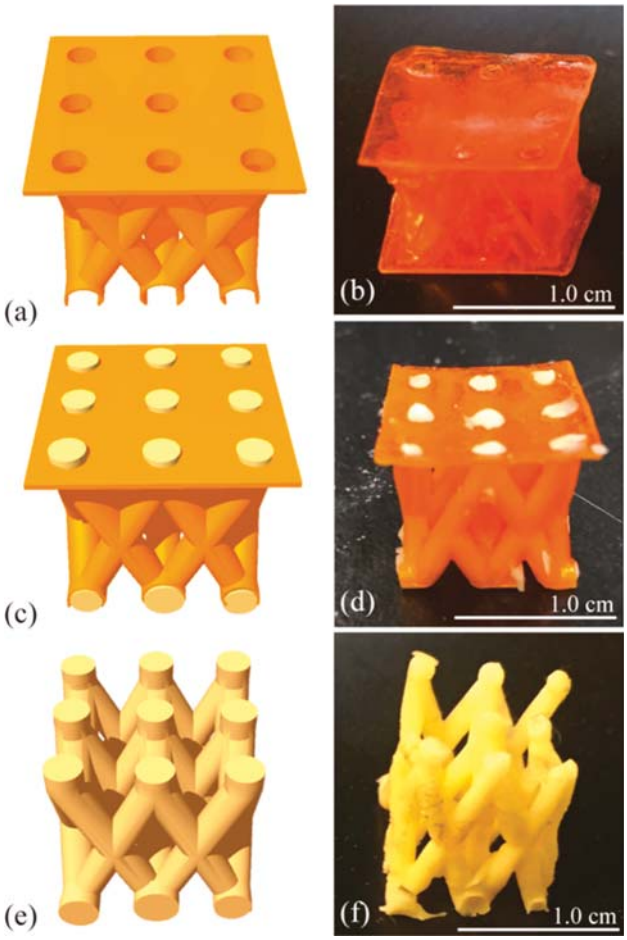

Figure 2. Fabrication of the biomimetic structures has three primary steps: (a/b) a hollow scaffold is 3D printed using projection microstereolithography, (c/d) a silicone elastomer is filled into the hollow scaffold and allowed to cure for 12 h, and (e/f) the hollow scaffold is dissolved away from the silicone using NaOH for 6 h.

DOI: 10.1021/acsbiomaterials.8b00349
ACS Biomater. Sci. Eng. 2018, 4, 1916−1923

cured for 12 h at 25 °C. The final step is to dissolve away the photoresin scaffold by placing the structure in a falcon tube containing 1 mol/L NaOH for 6 h. The elastomers are cleaned of excess resin and rinsed in DI water before testing (Figure 2e/f).

3.5. Compressive Testing. Compressive testing is used to characterize the response of the biomimetic structures and pancreatic tissue samples to mechanical loading and unloading. Due to the unique material composition and length scales of these two different sample types, different methods of compressive testing are performed based on the sample. The biomimetic structures are tested using an Instron Loadframe (Figure 3a) because the posts of the 3D printed structure

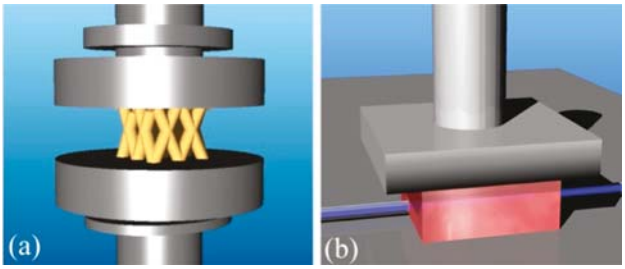

Figure 3. (a) Schematic of the Instron compressive testing setup with a rendering of the biomimetic structures. (b) Schematic of the OFPE testing setup with a pancreas sample.

have the potential to move, which would result in a nonuniform force on the OFPE sensor. The pancreatic tissues are tested using OFPE (Figure 3b) because the Instron cannot be transported and used in the BSL2+ environment required for porcine testing. Though they are tested using two different methods, the experimental parameters of compression are the same. Strains of 10%, 20%, and 30% are applied to each sample over a 30 s loading−unloading interval and increasing the strain rate increases the strain. This way, the results can be directly compared, even though different systems are used.

A schematic of the testing setup for the biomimetic structures is shown in Figure 3a. Compression rates of 0.067, 0.13, and 0.2 mm/s are used with a total interval of 30 s.

Compressive testing of the pancreatic tissue samples is conducted using OFPE. A schematic of the instrument is shown in Figure 3b. The pancreas samples are tested under identical conditions and strains as the biomimetic structures with compression rates of 0.033, 0.067, and 0.1 mm/s.

The OFPE method is based on the same principle as the Instron Loadframe with an optical fiber acting as the force sensor. Because the optical fiber is highly birefringent and polarization maintaining, the compressive force applied to the sample changes the way the light travels within the optical fiber, changing the polarization (ΔPol). By recording this change on a polarimeter, ΔPol vs Strain graphs, which are analogous to Stress vs Strain graphs, can be acquired. In addition, the optical fiber sensor offers improved spatial resolution over the loadframe's dashpot sensor. Given the heterogeneity of biomaterials, this improvement in resolution is critical. This system has been used to characterize a variety of biomaterials in the past.[23−25]

4. RESULTS AND DISCUSSION

4.1. Compressive Testing of Pancreatic Tissue. The results from compressive testing of pancreatic tissue using OFPE are shown in Figure 4. The loading curves result from compression of the tissue at 10%, 20%, and 30% strain. This testing protocol was previously demonstrated to be below the threshold of tissue damage.[25] The loading curves taken with the OFPE method demonstrate higher resolution than other methods. Therefore, in addition to the Young's modulus of the tissue, the buckling and hysteresis of the tissue can be resolved. Using these experimental results, we focus on reproducing the observed buckling characteristics through

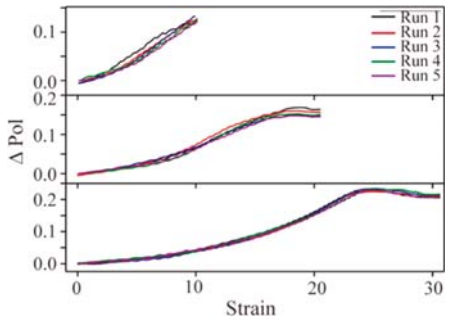

Figure 4. Mechanical testing results from compressive testing of pancreatic tissue with OFPE at 10%, 20%, and 30% strain. Key: Run 1 (black), Run 2 (red), Run 3 (blue), Run 4 (green), and Run 5 (purple).

modeling. In this sample, the buckling point of the pancreatic tissue at 30% strain is between 22 and 25% strain.

There are a multitude of structures within the tissue that could give rise to the observed buckling behavior. However, due to the nanoscale size of these structures and changes to the tissue over time, it is impossible to identify the structure that is primarily responsible for this behavior with conventional compression testing methods.[5,6]

To solve this challenge, we develop computational and biomimetic models based on the pathology, IHC, SHG, and SEM images of the tissue.[5,10−15,30] With these models, the geometry can be modified and used to determine the characteristics of the structures giving rise to the measured biomechanical behavior. The modeling results are compared to the results from compressive testing of the tissue to ensure that they align with the physiological parameters of buckling.

4.2. Modeling Results. FEA modeling of the structure is performed to understand the impact of changing the geometry and structure on the buckling behavior. Two different sets of geometric changes are modeled. The first set investigates the dependence of the mechanical behavior on the r ratio between the diameter and length (D/L) of the pillars. The second set investigates the impact of removing support pillars. Images from the FEA modeling of one of the biomimetic structures (D/L = 0.21) are presented in Figure 5. FEA images from additional structures are included in the supplement. For all of the geometries modeled, as the strain increases, the response of the structure changes. At the strain values studied in the present work, the structures do not experience irreversible damage.

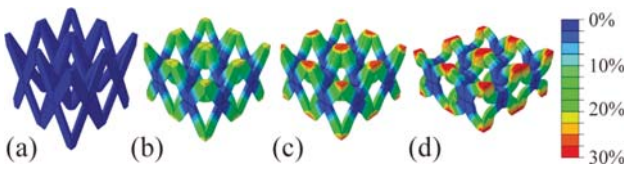

Figure 5. Images from FEA simulation of the buckling of a structure, with a ratio of D/L of 0.21. As increasing strain is applied to the structure buckling begins to occur. Buckling of this structure occurs around 30% strain. The structure undergoes several unique regions (a) before compression occurs, (b) during compression before buckling, (c) buckling occurs, and (d) buckling has occurred. The quantitative scale represents the strain on the structure between 0% and 30%. Key: 0% strain (blue), 10% strain (aqua), 20% strain (green), 30% strain (red).

DOI: 10.1021/acsbiomaterials.8b00349
ACS Biomater. Sci. Eng. 2018, 4, 1916−1923

Using the FEA model, we plot the stress vs strain within a suite of five structures with different D/L ratios (Figure 6a).

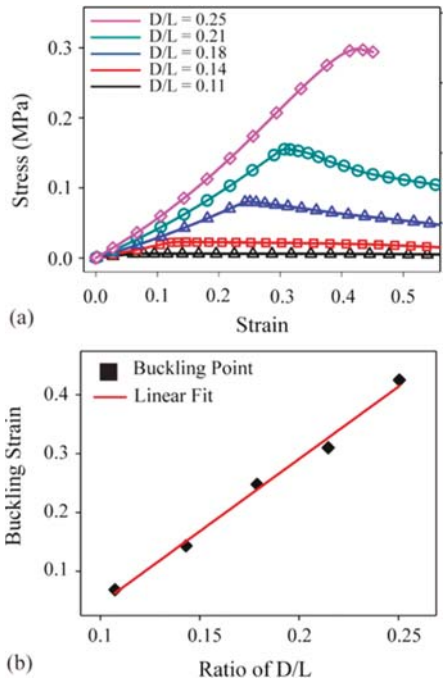

Figure 6. Simulation results for buckling characteristics of five biomimetic structures. (a) Loading curves for five simulated structures with variable D/L ratios. Key: D/L = 0.25 (purple), D/L = 0.21 (green), D/L = 0.18 (blue), D/L = 0.14 (red), D/L = 0.11 (black). (b) A linear fit is applied to the buckling strain for the five simulated structures vs the D/L ratio. Note the model stops at 0.45 strain for the structure with D/L = 0.25 because the model can no longer reach convergence at that point. Key: buckling point (black squares), linear fit (red line).

The D/L ratios modeled vary between 0.11 and 0.25. These values are selected based on published images of the pancreatic ECM plus additionally values that are larger and smaller to fully map out the size range.[5,10−15,30] In all five structures modeled, there is a clear buckling point. Over the D/L range studied, the dependence of the buckling point on D/L is linear (Figure 6b).

Using the FEA model, we plot the stress vs strain within a suite of six structures with different configurations of support beams along one face (Figure 7g). The geometries of these structures are shown in Figure 7a-7f, where the red beams represent the beams that have been removed. For this suite of structures, the D/L is fixed at 0.25. Despite the changes in geometry, the buckling point remains fairly constant, varying from 0.23 to 0.24 (Figure 7g). However, the maximum stress that can be applied to the structure varies from 0.39 to 0.51 MPa. The change in the maximum stress is directly related to the number of pillars that are removed. The structure with all of the support pillars removed has the lowest stress when it buckles, and the structure with all of the support pillars intact has the highest stress when it buckles. Structure (e) represents the buckling characteristics most similar to the physiological limits of buckling set by our porcine pancreatic tissue testing (Figure 4).

4.3. Compressive Testing of the Biomimetic Structures. The results from the compressive testing of the biomimetic structure depicted in Figure 7e, where two adjacent

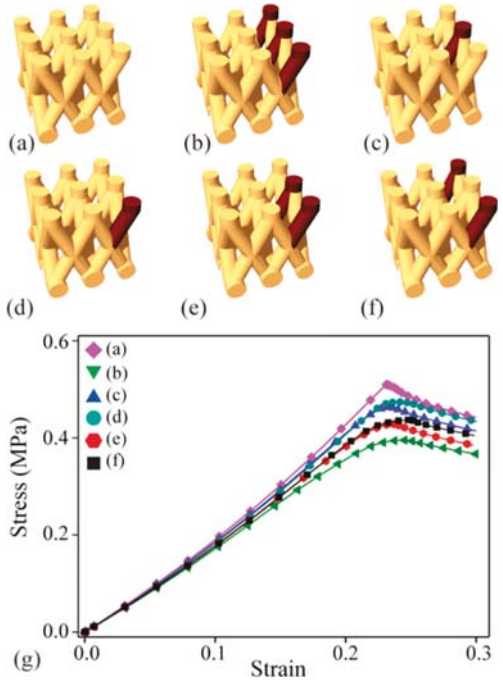

Figure 7. A suite of six silicone elastomer structures with known defects is fabricated. The structures are modified by removing the support beams of one of the faces of the symmetric structure to demonstrate how changing the fundamental structure impacts load bearing. The support beams, which have been removed, are indicated in red. (a) Structure where all the support beams remain intact. (b) Structure where all the support beams are removed. (c) Structure where the middle support beam is removed. (d) Structure where one outer support beam is removed. (e) Structure where both the middle support beam and one outer support beam are removed. (f) Structure where both the outer support beams are removed. (g) Simulation results for buckling characteristics of the six structures fabricated. This figure represents the loading curves for all six structures with a constant D/L ratio of 0.25 generated using our ABQUS model. Key: (a) purple diamond, (b) green triangle, (c) blue triangle, (d) teal circle, (e) red hexagon, (f) black square.

beams are removed, are plotted in Figure 8. Graphs from all six structures printed and compressively tested are included in the supplement. There is good reproducibility between subsequent runs of the same sample at each strain. Deviations are primarily attributed to movement of the sample on the platform between

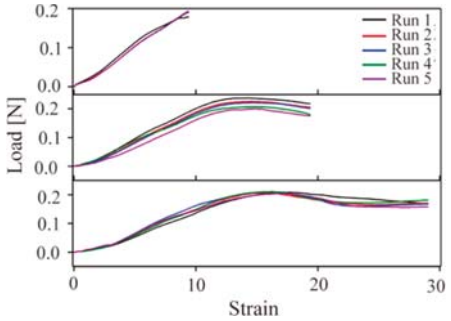

Figure 8. Mechanical testing results from using an Instron to compressively test the biomimetic structure depicted in Figure 7e at 10%, 20%, and 30% strain. Key: Run 1 (black), Run 2 (red), Run 3 (blue), Run 4 (green), and Run 5 (purple).

DOI: 10.1021/acsbiomaterials.8b00349
ACS Biomater. Sci. Eng. 2018, 4, 1916−1923

runs because the sample is not attached to the Instron stage. While attaching the sample can reduce movement, it can also introduce other artifacts into the measurement.

Differences in the exact buckling strain between the experimental structure and the modeled structures are due, in part, to differences in D/L throughout the structure. Experimentally controlling the D/L ratio is challenging because the final step of fabrication involves dissolving the support scaffold in 1 mol/L NaOH. This process can slightly modify the size of the molded structure. Alternative methods to improve the fabrication consistency are currently under investigation. For the purpose of this research, the reproducibility, the impact of D/L ratio, and the impact of geometry on the buckling strain are more significant than the exact value of the buckling point.

The buckling points are consistent between subsequent runs of the same experimental conditions on the same biomimetic structure. The buckling occurs at the same point within consecutive runs because the individual components of the structure can bend and return to their original configuration. None of the structures exhibit damage in response to repeated compressive loading. The difference in buckling point for each structure is attributed to the unique geometry of the structure.

4.4. Comparison of Pancreatic Tissue and Biomimetic Structure Results. While the biomimetic structures are an order of magnitude larger than the microstructures in the pancreatic tissue, both the observed buckling behavior and general mechanical response in this strain regime are extremely similar. This is due to the similar geometry of both structures. In both the biomimetic structures and the pancreas, there are several points where the structure can bend without breaking. Within the pancreas, this response is due to the geometry of the ECM that surrounds the acinar cells, which is reproduced by the beams of the biomimetic structures. The acinar cells create multicellular structures that look similar to clusters of berries and comprise the majority of the pancreas. Each acinar cell is an ellipse that connects to the intercalated duct.[38] Therefore, the acinar cells lie adjacent to one another but are only connected at a singular point. This directly corresponds to the biomimetic structure with a single support beam at one end of the structure.

To understand the parallels between our tissue and the biomimetic structures, the buckling point of five different pancreatic tissue samples determined with OFPE is plotted on the linear fit of our FEA model (Figure 9). Using the FEA results as a calibration curve, we are able to approximate the D/L ratio of the pancreatic tissue samples. Based on our experimental results, buckling occurs between 22 and 25% strain. Therefore, our D/L ratio values fall between 0.16 and 0.18. This provides us with a quantitative method for understanding the buckling within biomaterials.

Using the results from the fit in Figure 9, we can compare the OFPE results for the tissue to the biomechanical behavior of the different tissue components. As a rule, the ECM has been established as the primary contributing factor to the biomechanical behavior of different tissues.[16] By using published imaging results, we determine the D/L ratio of different ECM components in pancreatic tissue.[5,10−15,30,39−41] The ECM structure with a D/L value most similar to the system modeled is the collagen IV.[41] Collagen IV comprises the basement membrane of pancreatic tissue.[30] These structures have been well characterized and are generally described as a chicken wire or honeycomb structure providing the framework for cell-to-cell adhesion.[30,39−41] The relative scale described, as well as the known relationship between the acinar cells, fits within our imaging, modeling, and biomimetic structural results.

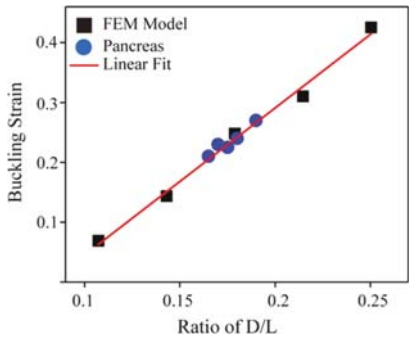

Figure 9. Plot of the pancreatic tissue data on the theoretical results of the buckling point versus the D/L ratio. This method provides us with a method for quantifying what is occurring within our biological tissues and understanding the mechanical behavior of the extracellular matrix of the tissue. Key: FEA Model (black square), OFPE Results (blue circle), Linear Fit (red line).

Current analytical and computational models have been unable to fully explain the biomechanical characteristics of tissues.[16,31] The limitation of existing methods is in part due to the fact that the structures of the ECM are nonuniform and are comprised of multiple materials.[42] By combining our experimental results from pancreatic tissues with dynamic computational and 3D printed models, we are able to develop a method that provides an unprecedented way of understanding the impact of the ECM geometry on the mechanical behavior of tissue.

5. CONCLUSION

In conclusion, we have demonstrated the ability to correlate biomimetic structures to the microstructure of biological tissues analyzed using nondestructive OFPE. This approach enables us to perform studies on the impact of the geometry of the ECM structure on the biomechanical characteristics of the tissue. Using this new method, we are able to correlate specific geometric features to biologically relevant microarchitectures in porcine pancreatic tissue.

Moving forward, this approach will facilitate a deeper understanding of the mechanical properties of tissues. In turn, this will enable researchers and clinicians to investigate and understand the complex role of ECM geometry in the biomechanical properties of tissues. By improving our understanding of how mechanical changes are associated with disease pathology, new approaches for therapeutics and diagnostics can be designed and developed. Eventually, these models may be tailored to specific patients to track the progression of biomechanical characteristics of their tissues as diseases progress. Due to the fact that changes in the structure of tissues are nearly ubiquitous across all disease pathologies, this method is promising in understanding both chronic and acute diseases.[1−4,7]

■ ASSOCIATED CONTENT

Supporting Information

The Supporting Information is available free of charge on the ACS Publications website at DOI: 10.1021/acsbiomaterials.8b00349.

DOI: 10.1021/acsbiomaterials.8b00349
ACS Biomater. Sci. Eng. 2018, 4, 1916−1923

Additional information regarding the modeling of the 3D printed structures and loading−unloading curves from mechanical testing of all the 3D printed structures (PDF)

AUTHOR INFORMATION

Corresponding Author

*E-mail: armani@usc.edu.

ORCID

Alexa W. Hudnut: 0000-0001-7774-388X

Andrea M. Armani: 0000-0001-9890-5104

Funding

This work was supported by the Office of Naval Research [N00014-11-1-0910, N00014-17-2270], the National Science Foundation [NSF Grant No. 1649093], A. E. Mann Graduate Research Fellowship, and the Zumberge Research Fund.

Notes

The authors declare no competing financial interest.

ACKNOWLEDGMENTS

The authors thank R. A. Arboleda, N. Katkhouda, B. Larson, S. Liu, and S. Mumenthaler.

ABBREVIATIONS

2D, two dimensional; 3D, three dimensional; FEA, finite element analysis; bTBI, blast induced traumatic brain injury; ECM, extracellular matrix; IHC, immunohistochemistry; SHG, second harmonic generation imaging; SEM, scanning electron microscopy; AFM, atomic force microscopy; OFPE, optical fiber polarimetric elastography; UV, ultraviolet; IACUC, Institutional Animal Care and Use Committee; RPMI, Roswell Park Memorial Institute Cell Culture Medium; DMEM, Dulbecco's Modified Eagle Medium; H&E, hematoxylin and eosin; *D*, diameter; *L*, length; *D*/*L*, ratio of diameter to length; NaOH, sodium hydroxide; DI, deionized; BSL2+, biosafety level 2 enhanced; ΔPol, Change in polarization

REFERENCES

(1) Janmey, P. A.; Miller, R. T. Mechanisms of mechanical signaling in development and disease. *J. Cell Sci.* **2011**, *124* (1), 9−18.

(2) Erkan, M.; Hausmann, S.; Michalski, C. W.; Fingerle, A. A.; Dobritz, M.; Kleeff, J.; Friess, H. The role of stroma in pancreatic cancer: diagnostic and therapeutic implications. *Nat. Rev. Gastroenterol. Hepatol.* **2012**, *9* (8), 454−467.

(3) Feig, C.; Gopinathan, A.; Neesse, A.; Chan, D. S.; Cook, N.; Tuveson, D. A. The pancreas cancer microenvironment. *Clin. Cancer Res.* **2012**, *18* (16), 4266−4276.

(4) Cecelja, M.; Chowienczyk, P. Role of arterial stiffness in cardiovascular disease. *JRSM Cardiovascular Disease* **2012**, *1* (4), 1.

(5) Laklai, H.; Miroshnikova, Y. A.; Pickup, M. W.; Collisson, E. A.; Kim, G. E.; Barrett, A. S.; Hill, R. C.; Lakins, J. N.; Schlaepfer, D. D.; Mouw, J. K.; LeBleu, V. S.; Roy, N.; Novitskiy, S. V.; Johansen, J. S.; Poli, V.; Kalluri, R.; Iacobuzio-Donahue, C. A.; Wood, L. D.; Hebrok, M.; Hansen, K.; Moses, H. L.; Weaver, V. M. Genotype tunes pancreatic ductal adenocarcinoma tissue tension to induce matricellular fibrosis and tumor progression. *Nat. Med.* **2016**, *22* (5), 497−505.

(6) Lee, G. Y. H.; Lim, C. T. Biomechanics approaches to studying human diseases. *Trends Biotechnol.* **2007**, *25* (3), 111−118.

(7) Bar-Kochba, E.; Scimone, M. T.; Estrada, J. B.; Franck, C. Strain and rate-dependent neuronal injury in a 3D in vitro compression model of traumatic brain injury. *Sci. Rep.* **2016**, *6*, 30550.

(8) Frantz, C.; Stewart, K. M.; Weaver, V. M. The extracellular matrix at a glance. *J. Cell Sci.* **2010**, *123* (24), 4195−4200.

(9) Bate-Smith, E. C.; Bendall, J. R. Factors determining the time course of rigor mortis. *J. Physiol.* **1949**, *110* (1−2), 47−65.

(10) Baskin, D. G. A Historical Perspective on the Identification of Cell Types in Pancreatic Islets of Langerhans by Staining and Histochemical Techniques. *J. Histochem. Cytochem.* **2015**, *63* (8), 543−558.

(11) Drifka, C. R.; Loeffler, A. G.; Mathewson, K.; Mehta, G.; Keikhosravi, A.; Liu, Y.; Lemancik, S.; Ricke, W. A.; Weber, S. M.; Kao, W. J.; Eliceiri, K. W. Comparison of Picrosirius Red Staining With Second Harmonic Generation Imaging for the Quantification of Clinically Relevant Collagen Fiber Features in Histopathology Samples. *J. Histochem. Cytochem.* **2016**, *64* (9), 519−529.

(12) Schenke-Layland, K. Non-invasive multiphoton imaging of extracellular matrix structures. *J. Biophotonics* **2008**, *1* (6), 451−462.

(13) Li, Y.; Trivedi, V.; Truong, T. V.; Koos, D. S.; Lansford, R.; Chuong, C.-M.; Warburton, D.; Moats, R. A.; Fraser, S. E. *Nat. Commun.* **2015**, *6*, 6798.

(14) Zheng, W.; ZhuGe, Q.; Zhong, M.; Chen, G.; Shao, B.; Wang, H.; Mao, X.; Xie, L.; Jin, K. Neurogenesis in Adult Human Brain after Traumatic Brain Injury. *J. Neurotrauma* **2013**, *30* (22), 1872−1880.

(15) Brissova, M.; Fowler, M. J.; Nicholson, W. E.; Chu, A.; Hirshberg, B.; Harlan, D. M.; Powers, A. C. Assessment of Human Pancreatic Islet Architecture and Composition by Laser Scanning Confocal Microscopy. *J. Histochem. Cytochem.* **2005**, *53* (9), 1087−1097.

(16) Fung, Y.-c. *Biomechanics: mechanical properties of living tissues*; Springer Science & Business Media: 1981; DOI: 10.1118/1.595186.

(17) Fu, H.; Xu, S.; Xu, R.; Jiang, J.; Zhang, Y.; Rogers, J. A.; Huang, Y. Lateral buckling and mechanical stretchability of fractal interconnects partially bonded onto an elastomeric substrate. *Appl. Phys. Lett.* **2015**, *106* (9), 091902.

(18) Middendorf, J. M.; Shortkroff, S.; Dugopolski, C.; Kennedy, S.; Siemiatkoski, J.; Bartell, L. R.; Cohen, I.; Bonassar, L. J. In vitro culture increases mechanical stability of human tissue engineered cartilage constructs by prevention of microscale scaffold buckling. *J. Biomech.* **2017**, *64* (Supplement C), 77−84.

(19) Ayyildiz, M.; Cinoglu, S.; Basdogan, C. Effect of normal compression on the shear modulus of soft tissue in rheological measurements. *J. Mech. Behav. Biomed. Mater.* **2015**, *49*, 235−243.

(20) Arda, K.; Ciledag, N.; Aktas, E.; Arıbas, B. K.; Köse, K. Quantitative Assessment of Normal Soft-Tissue Elasticity Using Shear-Wave Ultrasound Elastography. *AJR, Am. J. Roentgenol.* **2011**, *197* (3), 532−536.

(21) Kennedy, B. F.; Liang, X.; Adie, S. G.; Gerstmann, D. K.; Quirk, B. C.; Boppart, S. A.; Sampson, D. D. In vivo three-dimensional optical coherence elastography. *Opt. Express* **2011**, *19* (7), 6623−6634.

(22) Cross, S. E.; Jin, Y. S.; Rao, J.; Gimzewski, J. K. Nanomechanical analysis of cells from cancer patients. *Nat. Nanotechnol.* **2007**, *2* (12), 780−783.

(23) Hudnut, A. W.; Armani, A. M. High-resolution analysis of the mechanical behavior of tissue. *Appl. Phys. Lett.* **2017**, *110* (24), 243701.

(24) Harrison, M. C.; Armani, A. M. Portable polarimetric fiber stress sensor system for visco-elastic and biomimetic material analysis. *Appl. Phys. Lett.* **2015**, *106* (19), 191105.

(25) Hudnut, A. W.; Babaei, B.; Liu, S.; Larson, B. K.; Mumenthaler, S. M.; Armani, A. M. Characterization of the mechanical properties of resected porcine organ tissue using optical fiber photoelastic polarimetry. *Biomed. Opt. Express* **2017**, *8* (10), 4663−4670.

(26) Park, J.; Wang, S.; Li, M.; Ahn, C.; Hyun, J. K.; Kim, D. S.; Kim, D. K.; Rogers, J. A.; Huang, Y.; Jeon, S. *Nat. Commun.* **2012**, *3*, 916.

(27) Shan, S.; Kang, S. H.; Raney, J. R.; Wang, P.; Fang, L.; Candido, F.; Lewis, J. A.; Bertoldi, K. Multistable Architected Materials for Trapping Elastic Strain Energy. *Adv. Mater.* **2015**, *27* (29), 4296−4301.

(28) Miller, J. S.; Stevens, K. R.; Yang, M. T.; Baker, B. M.; Nguyen, D.-H. T.; Cohen, D. M.; Toro, E.; Chen, A. A.; Galie, P. A.; Yu, X.; Chaturvedi, R.; Bhatia, S. N.; Chen, C. S. Rapid casting of patterned vascular networks for perfusable engineered three-dimensional tissues. *Nat. Mater.* **2012**, *11* (9), 768−774.

DOI: 10.1021/acsbiomaterials.8b00349
ACS Biomater. Sci. Eng. 2018, 4, 1916−1923

(29) Jiang, Y.; Wang, Q. Highly-stretchable 3D-architected mechanical metamaterials. *Sci. Rep.* **2016**, *6*, 34147.
(30) Vigier, S.; Gagnon, H.; Bourgade, K.; Klarskov, K.; Fülöp, T.; Vermette, P. Composition and organization of the pancreatic extracellular matrix by combined methods of immunohistochemistry, proteomics and scanning electron microscopy. *Current Research in Translational Medicine* **2017**, *65* (1), 31−39.
(31) Babaei, B.; Velasquez-Mao, A. J.; Thomopoulos, S.; Elson, E. L.; Abramowitch, S. D.; Genin, G. M. Discrete quasi-linear viscoelastic damping analysis of connective tissues, and the biomechanics of stretching. *J. Mech. Behav. Biomed. Mater.* **2017**, *69*, 193−202.
(32) Mulliken, A. D.; Boyce, M. C. Mechanics of the rate-dependent elastic−plastic deformation of glassy polymers from low to high strain rates. *Int. J. Solids Struct.* **2006**, *43* (5), 1331−1356.
(33) Gibson, R. F. A review of recent research on mechanics of multifunctional composite materials and structures. *Composite Structures* **2010**, *92* (12), 2793−2810.
(34) Yeoh, O. Some forms of the strain energy function for rubber. *Rubber Chem. Technol.* **1993**, *66* (5), 754−771.
(35) Shahzad, M.; Kamran, A.; Siddiqui, M. Z.; Farhan, M. Mechanical Characterization and FE Modelling of a Hyperelastic Material. *Mater. Res.* **2015**, *18*, 918−924.
(36) Spek, A. Structure validation in chemical crystallography. *Acta Crystallogr., Sect. D: Biol. Crystallogr.* **2009**, *65* (2), 148−155.
(37) Liska, R.; Schwager, F.; Maier, C.; Cano-Vives, R.; Stampfl, J. Water-soluble photopolymers for rapid prototyping of cellular materials. *J. Appl. Polym. Sci.* **2005**, *97* (6), 2286−2298.
(38) Kasper, D.; Fauci, A.; Hauser, S.; Longo, D.; Jameson, J. *Harrison's Principles of Internal Medicine*; McGraw-Hill Education: New York, 2015; DOI: 10.1212/01.WNL.0000161672.02235.A0.
(39) Öhlund, D.; Franklin, O.; Lundberg, E.; Lundin, C.; Sund, M. Type IV collagen stimulates pancreatic cancer cell proliferation, migration, and inhibits apoptosis through an autocrine loop. *BMC Cancer* **2013**, *13*, 154−154.
(40) Gress, T.; Menke, A.; Bachem, M.; Müller-Pillasch, F.; Ellenrieder, V.; Weidenbach, H.; Wagner, M.; Adler, G. Role of extracellular matrix in pancreatic diseases. *Digestion* **1998**, *59* (6), 625−637.
(41) Khoshnoodi, J.; Pedchenko, V.; Hudson, B. Mammalian Collagen IV. *Microsc. Res. Tech.* **2008**, *71* (5), 357−370.
(42) Shima, H. Buckling of Carbon Nanotubes: A State of the Art Review. *Materials* **2012**, *5* (1), 47.

DOI: 10.1021/acsbiomaterials.8b00349
ACS Biomater. Sci. Eng. 2018, 4, 1916−1923